Important Notice to Authors

No further publication processing will occur until we receive your response to this proof.

Attached is a PDF proof of your forthcoming article in PRB. Your article has 9 pages and the Accession Code is **BE14519**.

Please note that as part of the production process, APS converts all articles, regardless of their original source, into standardized XML that in turn is used to create the PDF and online versions of the article as well as to populate third-party systems such as Portico, Crossref, and Web of Science. We share our authors' high expectations for the fidelity of the conversion into XML and for the accuracy and appearance of the final, formatted PDF. This process works exceptionally well for the vast majority of articles; however, please check carefully all key elements of your PDF proof, particularly any equations or tables.

Figures submitted electronically as separate files containing color appear in color in the online journal. However, all figures will appear as grayscale images in the print journal unless the color figure charges have been paid in advance, in accordance with our policy for color in print (https://journals.aps.org/authors/color-figures-print).

Specific Questions and Comments to Address for This Paper

Q: This reference could not be uniquely identified due to incomplete information or improper format. Please check all information and amend if applicable.

ORCIDs: Please follow any ORCID links ( ) after the author names and verify that they point to the appropriate record for each author.

Open Funder Registry: Information about an article's funding sources is now submitted to Crossref to help you comply with current or future funding agency mandates. Crossref's Open Funder Registry (https://www.crossref.org/services/funder-registry/) is the definitive registry of funding agencies. Please ensure that your acknowledgments include all sources of funding for your article following any requirements of your funding sources. Where possible, please include grant and award ids. Please carefully check the following funder information we have already extracted from your article and ensure its accuracy and completeness:
National Science Foundation (US), NSF-1610953

Other Items to Check

- Please note that the original manuscript has been converted to XML prior to the creation of the PDF proof, as described above. Please carefully check all key elements of the paper, particularly the equations and tabular data.
- Title: Please check; be mindful that the title may have been changed during the peer-review process.
- Author list: Please make sure all authors are presented, in the appropriate order, and that all names are spelled correctly.
- Please make sure you have inserted a byline footnote containing the email address for the corresponding author, if desired. Please note that this is not inserted automatically by this journal.
- Affiliations: Please check to be sure the institution names are spelled correctly and attributed to the appropriate author(s).
- Receipt date: Please confirm accuracy.
- Acknowledgments: Please be sure to appropriately acknowledge all funding sources.
- Hyphenation: Please note hyphens may have been inserted in word pairs that function as adjectives when they occur before a noun, as in "x-ray diffraction," "4-mm-long gas cell," and "*R*-matrix theory." However, hyphens are deleted from word pairs when they are not used as adjectives before nouns, as in "emission by x rays," "was 4 mm in length," and "the *R* matrix is tested."

  Note also that Physical Review follows U.S. English guidelines in that hyphens are not used after prefixes or before suffixes: superresolution, quasiequilibrium, nanoprecipitates, resonancelike, clockwise.
- Please check that your figures are accurate and sized properly. Make sure all labeling is sufficiently legible. Figure quality in this proof is representative of the quality to be used in the online journal. To achieve manageable file size for online delivery, some compression and downsampling of figures may have occurred. Fine details may have become somewhat fuzzy, especially in color figures. The print journal uses files of higher resolution and therefore details may be sharper in print. Figures to be published in color online will appear in color on these proofs if viewed on a color monitor or printed on a color printer.
- Please check to ensure that reference titles are given as appropriate.
- Overall, please proofread the entire *formatted* article very carefully. The redlined PDF should be used as a guide to see changes that were made during copyediting. However, note that some changes to math and/or layout may not be indicated.

Ways to Respond

- ***Web:*** If you accessed this proof online, follow the instructions on the web page to submit corrections.

- ***Email:*** Send corrections to prbproofs@aptaracorp.com
  Subject: **BE14519** proof corrections
- ***Fax:*** Return this proof with corrections to +1.703.791.1217. Write **Attention:** PRB Project Manager and the Article ID, **BE14519**, on the proof copy unless it is already printed on your proof printout.

PHYSICAL REVIEW B **00**, 005400 (2021)

Abrikosov vortex corrections to effective magnetic field enhancement in epitaxial graphene

Luke R. St. Marie,[1,2] Chieh-I Liu,[1,3] I-Fan Hu,[1,4] Heather M. Hill,[1] Dipanjan Saha,[1] Randolph E. Elmquist,[1] Chi-Te Liang,[2] David B. Newell,[1] Paola Barbara,[2] Joseph A. Hagmann,[1] and Albert F. Rigosi[1,*]

[1]*Physical Measurement Laboratory, National Institute of Standards and Technology (NIST), Gaithersburg, Maryland 20899, USA*

[2]*Department of Physics, Georgetown University, Washington, DC 20057, USA*

[3]*Department of Chemistry and Biochemistry, University of Maryland, College Park, Maryland 20742, USA*

[4]*Department of Physics, National Taiwan University, Taipei 10617, Taiwan*

(Received 21 May 2021; revised 21 July 2021; accepted 16 August 2021; published xxxxxxxxxx)

Here, we report the effects of enhanced magnetic fields resulting from type-II superconducting NbTiN slabs adjacent to narrow Hall bar devices fabricated from epitaxial graphene. Observed changes in the magnetoresistances were found to have minimal contributions from device inhomogeneities, magnet hysteresis, electron density variations along the devices, and transient phenomena. We hypothesize that Abrikosov vortices, present in type-II superconductors, contribute to these observations. By determining the London penetration depth, coupled with elements of Ginzburg-Landau theory, one can approximate an upper bound on the effect that vortex densities at low fields (< 1T) have on the reported observations. These analyses offer insights into device fabrication and how to utilize the Meissner effect for any low-field and low-temperature applications using superconductors.

DOI: 10.1103/PhysRevB.00.005400

I. INTRODUCTION

Graphene has proven, in the last decade, to be a technologically useful material thanks to its extraordinary electrical properties [1–4]. Its low-field (< 3T) transport applications are far reaching, ranging from spintronics devices [5–7] to electron optics [8–11] to serving as a standard for resistance [12–16]. Moreover, graphene continues to offer research avenues in the lower-field regime, where its physics may be studied and implemented for the discovery and optimization of nanoscale and macroscopic devices.

One of the frequent requirements for measuring graphene-based devices for the transport applications listed above is the use of a magnetic field (B field) to activate or reveal certain effects. For low-field applications, commercially available permanent magnets can only exhibit a field as strong as 1 T. Such a limit could benefit from potential magnetic enhancement provided by the device being used. The Meissner effect in type-I superconductors could deliver significant enhancement in local areas due to B field screening but with the major disadvantage that all of these superconductors have critical fields well below 1 T. Consequently, for many practical applications, type-II superconductors provide more flexibility. Many efforts have been concerned with direct interactions of superconductors on or around graphene in the form of proximity effects, Andreev reflections, and device contacting [17–20], but fewer efforts report information on the extent to which B fields could be enhanced with superconductors [21,22].

In this paper, we investigate the effects of adjacent type-II superconducting NbTiN slabs on the measured resistances of narrow Hall bar devices fabricated from epitaxial graphene (EG) on 4*H*-SiC. Observed apparent changes in the magnetoresistances and, by extension, the electron densities suggest that the devices are experiencing an enhanced B field, whose transverse profile is analyzed in the context of the Meissner effect and Abrikosov vortices in type-II superconductors. The upper critical B field for the NbTiN slabs was determined with experimental data, enabling one to determine the London penetration depth (λ_L). When coupled with elements of Ginzburg-Landau (GL) theory, an approximation of the vortex densities in the low-field regime was calculable. The results and analyses presented here offer advancement in the application space of low-field, low-temperature technologies, where the local B-field enhancement can reduce future B-field requirements for a variety of devices.

II. EXPERIMENTAL AND NUMERICAL METHODS

A. Device preparation

EG films were grown on 4*H*-SiC substrates at a temperature of 1900 °C. This temperature enables Si atoms to sublimate from the substrate, allowing C atoms to form a hexagonal lattice. Substrates were diced from 4*H*-SiC(0001) wafers from CREE [23] and chemically cleaned with a 5:1 diluted solution of hydrofluoric acid and deionized water. Substrates were then processed with AZ5214E to utilize polymer-assisted sublimation [24]. Next, substrates were placed on a polished graphite slab (SPI Glas 22 [23]) silicon-face down. The growth furnace was flushed with argon gas and filled (100 kPa) from a 99.999% liquid argon source. The

*albert.rigosi@nist.gov, afr2117@columbia.edu

graphite-lined resistive-element furnace (Materials Research Furnaces Inc. [23]) was held at 1900 °C for ∼5 min, with respective heating and cooling rates of about 1.5 °C/s.

After the completion of the epitaxial growth procedure, EG films were inspected with optical and confocal laser scanning microscopy, as described by previous work [25]. For device fabrication, we followed well-documented photolithography processes designed for etching Hall bars and corresponding device contacts [26], using a layer of Pd/Au to protect the EG surface from organic contaminants. A key difference in our process was the use of NbTiN for the contact pad material, a decision made on the basis of the superconducting properties of this material [27,28]. A control device design is illustrated in Fig. 1(a), with the injected current intended to travel across the length of the device and the four pairs of orthogonal contacts intended for Hall resistance measurements. Before removing the protective Pd/Au layer from the EG, 1-μm-thick superconducting slabs composed of NbTiN were deposited on each side of the graphene Hall bar (150 μm wide, along various lengths), as illustrated in Fig. 1(b) and seen in final form in Fig. 1(c). Externally applied B fields between the lower and upper critical B fields of NbTiN are expected to deform around the slabs as magnetic flux incrementally penetrates the slab in the form of Abrikosov vortices, with the potential for flux pinning to occur due to impurities and disorder [29–31].

The last step for device preparation was the functionalization process to regulate the electron density without the need for a top gate. The compound $Cr(CO)_6$ was used in a custom, nitrogen-filled furnace at 130 °C. At this temperature, the compound breaks down and forms functional group $Cr(CO)_3$, which bonds to the EG surface in a way that does not degrade the electrical properties [32–35]. This step is crucial because it allows the electron density to remain low (on the order 10^{10} cm^{-2}) while stored in air and with uniform annealing, which supports a uniform electron density across the device. The variation across the entire chip is on the order of 10^{10} cm^{-2} [34], which is small compared with the typical values of inherent electron doping in EG of 10^{13} cm^{-2} [36]. The EG surface also typically hosts harmless particulates of oxidized chromium.

B. Device and superconductor characterization

A Janis Cryogenics cryostat was utilized for transport measurements [23]. All relevant data were collected at B-field values between 0 and ±5 T and at temperatures within the range 1.5–15 K and currents as high as 22 μA. Data from Hall resistance and longitudinal resistivity measurements were collected with lock-in amplifiers. The superconducting NbTiN slabs were characterized to determine several parameters beneficial for later analyses. The spacing between the slab edge and the EG edge was designed to be 5 μm. In Fig. 2(a), the NbTiN slab resistance was measured as a function of temperature using 1 μA of applied current, with the transition temperature determined to be ∼12.51 K by taking the midpoint between the 10 and 90% asymptotic normal-state resistance values.

Additional data on the upper critical field of the NbTiN slab are provided in the Supplemental Material [37]. In short,

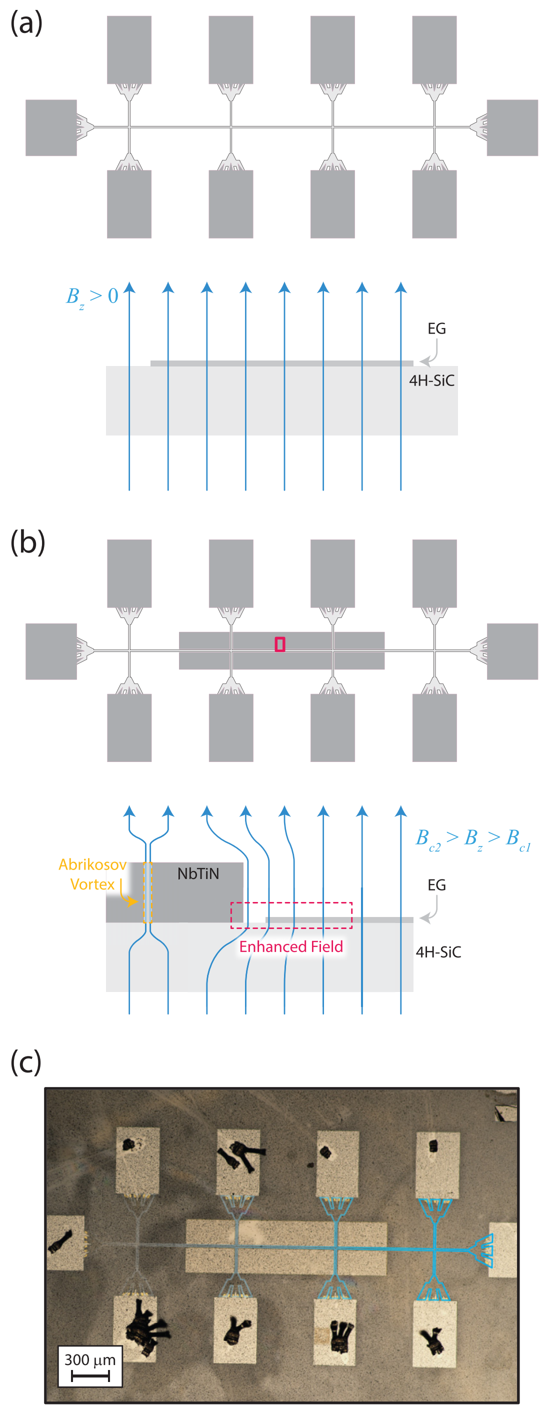

FIG. 1. (a) An illustration of the control device is provided. The length and width of the Hall bar device are ∼2 mm and 10 μm, respectively. A cross-section is shown below, and under normal applied B fields, field lines do not deviate. (b) An illustration of the device with the superconducting slabs is provided. The small red region indicates a magnification and cross-section shown just below. Along the top edge of the Hall bar within the regions surrounded by adjacent NbTiN slabs, the B field is expected to deform as a result of the type-II superconducting mixed state (lines represent B field, not flux quanta). (c) The optical image shows an example device that was measured, with a gradually fading light blue augmented outline showing the perimeter of the etched epitaxial graphene (EG). The appearance of dirt or residue is a result of the functionalization process.

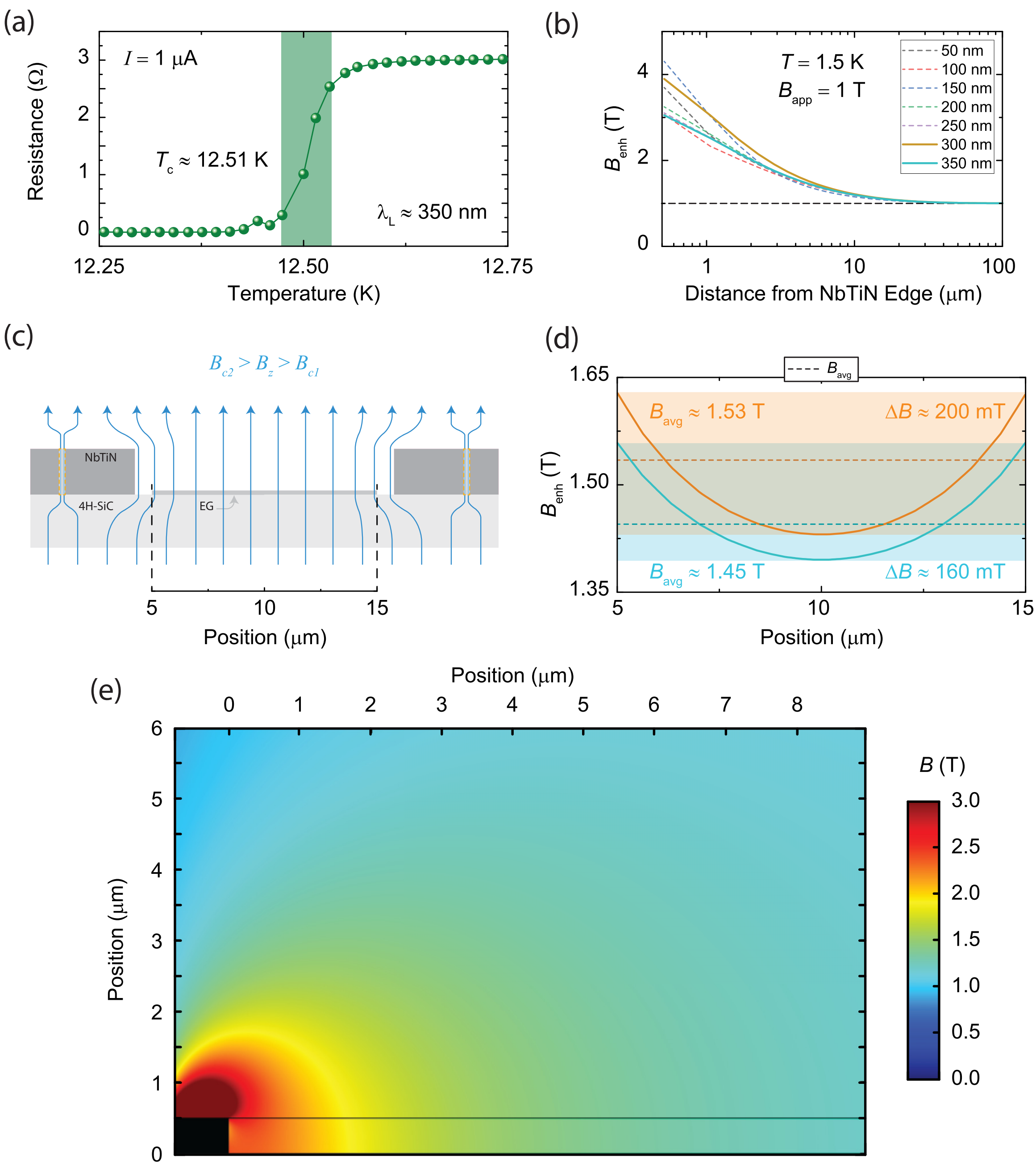

FIG. 2. (a) The NbTiN slab resistance was measured as a function of temperature using 1 μA, with the transition temperature determined to be ~12.5 K. (b) COMSOL simulations show the enhanced B field drop off away from the slab for different values of λ_L [23]. Simulations were performed at 1.5 K and 1 T. The two solid lines indicate the closer approximations to the determined λ_L. (c) An illustration of the B-field enhancement along the width of the device is provided, with the corresponding B-field profile shown in (d). (d) The B-field profiles for two λ_L (300 and 350 nm, in orange and light blue color themes, respectively) were simulated along the width of the device, giving an idea for the range of B-field variation and the average enhanced field. (e) A color map of the simulated enhanced B field along the cross-section of the device [dashed red box in Fig. 2(b)] was generated with COMSOL at 1 T, with the black box in the lower left corner indicating the end of the NbTiN slab and the epitaxial graphene (EG) film aligned with the bottom horizontal axis (starting at 5 μm) [23].

the approximation $B_{c2}(0) \approx 0.69\ T_c \frac{dB_{c2}}{dT}$ gives us an upper critical field (at 0 K) of 11.41 ± 1.02 T [38,39]. With the well-known condition of overlapping vortices occurring at the upper critical field in type-II superconductors $B_{c2} = \frac{\Phi_0}{2\pi\xi^2}$, one may determine the coherence length $\xi = 5.37 \pm 0.24$ nm. Given its relevance in later analyses, λ_L was determined by taking the reported value in the literature of the depairing current density in NbTiN [40–42]:

$$J_d(0) = \sqrt{\frac{2\Phi_0 B_{c2}(0)}{27\pi\mu_0^2 {\lambda_L}^4(0)}}. \tag{1}$$

Using the reported $J_d(0) = 1.5 \times 10^{11}$ A/m^2 and Φ_0 (2.0678×10^{-15} Wb), our $\lambda_L(0) \approx 354 \pm 8$ nm. This value

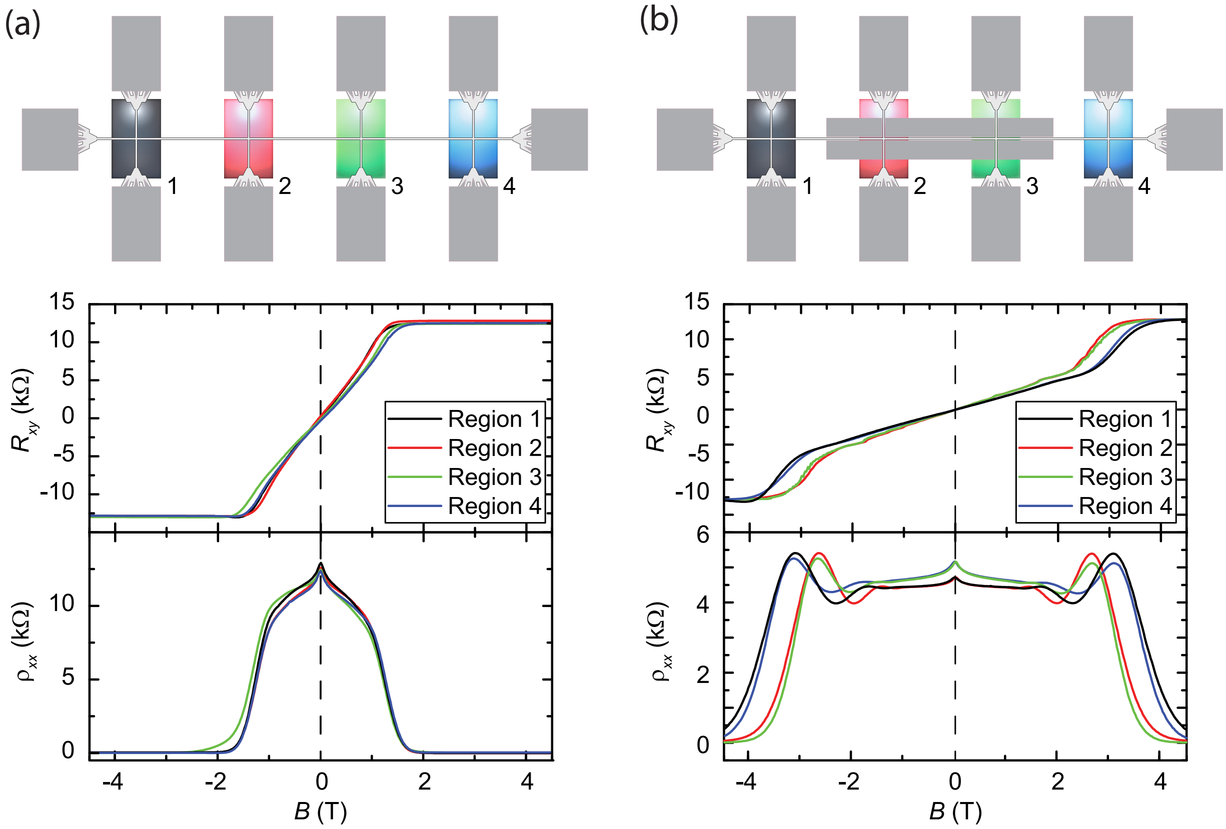

FIG. 3. (a) In the control device (top panel), the Hall resistances were measured in four regions, indicated by the corresponding color themes. By extension, their electron densities were determined using the low-field slope to verify device uniformity. The bottom panel shows the longitudinal resistivity curves. (b) In a device with the NbTiN slabs, the same four regions are measured, with a key difference being the apparent horizontal scaling of the Hall resistances for two regions adjacent to the NbTiN slabs. Longitudinal resistivity was measured from top contacts and bottom contacts for the regions 2 and 3 (red and green curves) and averaged between the top and bottom pairing of regions 1 and 4 (black and blue curves) with the source and drain contact. These data were collected at a different electron density to accentuate the effect of the presence of the NbTiN slab. All data were adjusted for magnet hysteresis (more information in the Supplemental Material [37]).

does not change significantly at our measurement temperature of 1.5 K since this is an order of magnitude below the NbTiN transition temperature. It thus follows that the approximate GL parameter $\kappa = \frac{\lambda}{\xi} \approx 66$.

C. COMSOL simulations

The cross-platform finite element analysis software COMSOL was employed for simulating the Meissner effect in NbTiN [23]. The model was constructed with cylindrical symmetry to prevent the complications that can occur in rectangular coordinates [43,44]. The layout may be seen in the Supplemental Material [37]. The applied B field for the simulations was 1 T, which assumed a perfect Meissner state in NbTiN. The component values in the calculated B-field vector array scale linearly with applied B field. The enhanced B-field strength along the direction away from the slab is shown in Fig. 2(b) as a function of distance for various λ_L. The two solid lines indicate the closer approximations to the determined λ_L. The drop-off of the magnetic field strength away from the NbTiN is approximately proportional to the reciprocal distance cubed, as can be found from a log-log plot of Fig. 2(b) and comparing with similar calculations [45].

An illustration and corresponding B-field enhancement is shown for the cross-section of the device in Figs. 2(c) and 2(d), respectively. For the cases of λ_L being ~300 nm (orange colors) or 350 nm (light blue colors), the average B fields were 1.53 and 1.45 T, respectively, and as indicated by the dotted lines, with corresponding variations of 200 and 160 mT. In Fig. 2(e), a color map of the enhanced B field in the cross-sectional area of the device edge was generated. Note that the horizontal axis origin starts at the slab edge (and the EG film at 5 μm on the horizontal axis and 0 μm on the vertical axis), whereas the vertical axis starts in the center of the slab.

III. OBSERVATION OF APPARENT MAGNETIC FIELD ENHANCEMENT

Transport measurements were performed on control and experimental devices, exemplified by the illustrations in Figs. 3(a) and 3(b), respectively. In the control device, Hall resistances were measured in four regions, indicated by the black, red, green, and blue curves. The slope of the Hall resistance at low field (<1T) was used to calculate the electron density: $n_e = \frac{1}{e(\frac{dR_{xy}}{dB})}$. The variation in the electron density is within the expected behavior, namely, on the order of 10^{10} cm^{-2} [34]. Corresponding longitudinal resistance data were also collected. In Fig. 3(b), a device with the NbTiN slabs had the same four regions measured. The presence of the NbTiN slabs is a key difference in the configuration for regions 2 and 3. For both sets of data, apparent horizontal scalings of the resistance curves were observed. All data were adjusted for magnet hysteresis (see the Supplemental Material [37]).

To better understand the forthcoming analysis of these data, a description of the physical phenomena behind all of these observations will be helpful. In the top data panel of Fig. 3(a), four distinct Hall resistances were measured simultaneously on the control device. These data appear to take on negative magnetoresistances because of the change in polarity of the B field. Ultimately, the experimental measurements were recording the voltages between the top and bottom sets of electrical contacts. As with typical quantum Hall effect data, the $\nu = 2$ plateaus appear to be at $\pm\frac{h}{2e^2}$. The resistance data are obtained by dividing the measured voltages by the applied current, and since the voltages adopt a negative value for negative B-field values, one should expect to see the data as they appear in both R_{xy} panels. For the data in the top panel of Fig. 3(b), all four Hall resistances no longer overlap within expected electron density variations. Rather, the data for regions 1 and 4 (no adjacent slab) describe a similar electron density, whereas the data for regions 2 and 3, though matching in shape, describe a device with a different electron density (determined by the slope at low field, as seen above). For Fig. 3(b), the device was adjusted so that data were acquired at a different electron density than in Fig. 3(a) to accentuate the effects of the adjacent NbTiN slab. That is, at lower electron densities, the effect is still visible but more susceptible to experimental error due to the natural electron density variation across the device [34].

By focusing on the bottom data panels of Figs. 3(a) and 3(b), one may extract a similar conclusion with the measured longitudinal resistivities. The notable observation for the longitudinal resistivity is that, when measuring the voltage between two adjacent electrical contacts within the region near the NbTiN slab, the resulting resistivity also appears horizontally contracted [red and green curves of Fig. 3(b)] with respect to a longitudinal resistivity determined outside of the affected regions. At lower electron densities, like that in Fig. 3(a), the longitudinal resistivity remains subdued, having only a major peak near zero field [34]. However, at higher electron densities, the emergence of Shubnikov–de Haas oscillations becomes prominent, manifesting as side peaks in the magnetoresistance [46]. The electron density may also be estimated from the periodicity of these oscillations, but such estimations are not as accurate in this case as those estimated from the linearity of the Hall response. A very rough estimate of the horizontal scaling factor for both the Hall resistance and longitudinal resistivity may be estimated by simple contraction of the horizontal axis for the data taken in the regions not adjacent to the NbTiN slab and in this case is ∼15%. The question then becomes one of determining the cause of the observed scaling.

Two possible sources for the changes in the resistance vs B-field curves could include device inhomogeneity and transient effects. As a reaffirmation, all devices were checked for linearity in their zero-field current-voltage (I-V) responses (a set of which is available in the Supplemental Material [37]). After confirming this behavior, transient effects were analyzed by ramping the magnetic field in steps of 0.1 T while measuring the two resistances over a span of several time constants corresponding to the equilibrating response. This resulted in a time-dependent resistance measurement and a parametric plot of the B-field-dependent resistance (both of which are in the Supplemental Material [37]). The effects of any transient phenomena were thus characterized and represented by an uncertainty that became applicable to all resistance measurements.

In Fig. 4(a), several Hall resistances and electron densities were measured for both types of regions (with and without NbTiN slabs). The data taken in regions without the slabs are shown as dotted lines and labeled as *actual*, indicating the lack of external effects on expected control measurements. For the corresponding regions adjacent to the slabs, data curves are plotted as solid curves labeled as *apparent* with a shaded region indicating the 1σ uncertainty associated with electron density variation and transient effects. This shading is only presented for this graph to grant clarity in the remaining figures. The corresponding longitudinal resistances are shown in Fig. 4(b) and verify the apparent scaling factor present within the regions near NbTiN slabs.

One may intuitively gather that a superconductor in the pure Meissner state (and to a smaller extent, a mixed state) would expel B fields, possibly contributing to the apparent scaling. In Figs. 4(c) and 4(d), temperature-dependent Hall resistance and longitudinal resistivity data for a fixed electron density were compared, respectively. The agreement of the actual and apparent data (within experimental uncertainty) for measurements at higher temperatures approaching T_c suggests that the NbTiN superconducting state is contributing to the observed scaling.

IV. ABRIKOSOV VORTEX CORRECTIONS

A. Comparing pure and mixed states

To better quantify the aforementioned observations, Hall resistance data for a fixed electron density from regions with and without NbTiN slabs were compared to yield the fractional differences in Hall resistances [Fig. 5(a)]. The light blue region indicates the bounds of what we are calling low field since higher fields contribute nonlinearly to changes in the electron density. To calculate electron densities with low B-field resistance measurements, the B-field bounds are roughly ±2 T. In Fig. 5(b), the difference in the actual and apparent responses yield an average "enhancement" factor of ∼16.3%. This average was determined from low-field data and is labeled as an enhancement factor for consistency with what should be a stronger magnetic field near the NbTiN slabs. To understand the extent of this enhancement, another set of Hall resistance data was simulated by scaling the actual data with the expected average magnetic field across the width of the device determined by the pure Meissner state case in Figs. 2(d) and 2(e). All of these curves are shown in Fig. 5(c), with the actual and apparent cases shown as gold

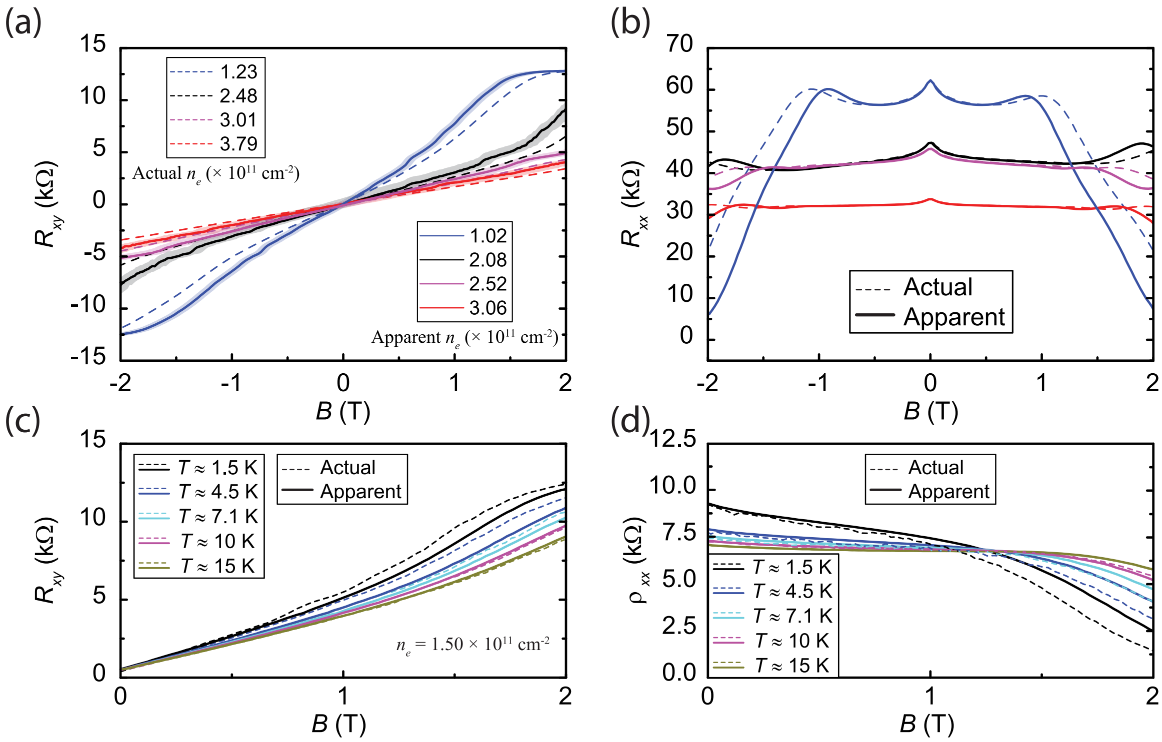

FIG. 4. (a) Several Hall resistances were measured for regions with and without nearby NbTiN slabs. Data taken in regions without the slabs are shown as dotted lines (actual). For corresponding regions adjacent to the slabs, data curves are shown as solid with a shaded region indicating the 1σ uncertainty associated with electron density variation and transient effects. (b) Longitudinal resistances were measured to verify the apparent scaling factor present within the regions adjacent to NbTiN slabs. (c) Hall and (d) longitudinal resistance data for one electron density were compared at several temperatures, with one being above T_c for NbTiN.

and red curves, respectively, and the pure Meissner, simulated resistance curve shown as a dotted blue curve.

Another way to justify our low-field limitations to these analyses can be seen in Figs. 5(d)–5(f). The first derivatives for each of three Hall resistance measurements at three fixed electron densities are shown, and though the flatness is not ideal, it is evident that the characteristic linearity of actual data is only reliable for determining the electron density, and by extension, any clean contributions to local B-field enhancement, for B fields within ± 1 T. Nonetheless, one may continue to analyze low-field data for learning more about the contributions of Abrikosov vortices on the observed B-field enhancement.

B. Vortex contributions

To gain a better understanding for how Abrikosov vortices are behaving at low fields and to attribute some density of vortices with our observations, we begin with the GL equations [Eqs. (2) and (3)]:

$$\frac{1}{2m}\left(\frac{\hbar}{i}\nabla - \frac{e}{c}\mathbf{A}\right)^2 \psi + \alpha\psi + \beta|\psi|^2\psi = 0, \qquad (2)$$

$$\mathbf{J} = \frac{c}{4\pi}\nabla \times \mathbf{B} = \frac{e\hbar}{2mi}(\psi^*\nabla\psi - \psi\nabla\psi^*) - \frac{e^2}{mc}\psi^*\psi\mathbf{A}. \quad (3)$$

Within this discussion, we define all variables as such: m (mass), e (elementary charge), c (speed of light), ψ (wave function, with corresponding radial component f and long-distance coefficient ψ_∞), α and β (phenomenological parameters), $\mathbf{J}$ (current density), $\mathbf{B}$ (magnetic field), $\mathbf{A}$ (vector potential), and Φ_0 (magnetic flux quantum). A vortex can be described by the following wave function: $\psi = \psi_\infty f(r) e^{i\theta}$. When used in conjunction with a nonsingular variation of the London gauge potential, simplifying the GL equations yields [46]

$$f - f^3 - \xi^2\left[\left(\frac{1}{r} - \frac{2\pi A}{\Phi_0}\right)^2 f - \frac{1}{r}\frac{d}{dr}\left(r\frac{df}{dr}\right)\right] = 0, \qquad (4)$$

$$\mathbf{J} = \frac{e\hbar}{m}\psi_\infty^2 f^2\left(\frac{1}{r} - \frac{2\pi A}{\Phi_0}\right). \qquad (5)$$

The reason for pointing out these formulations is because, in many instances of discussing a vortex, one typically only concerns oneself with the B-field surrounding and far from the core (which has a radius of about ξ). For these cases, it is well known that f can be approximated as unity, and solving for Eqs. (4) and (5) yields a final vortex B field of [47]

$$\mathbf{B}(r) = \frac{\Phi_0}{2\pi\lambda^2}K_0\left(\frac{r}{\lambda}\right). \qquad (6)$$

In Eq. (6), K_0 is a modified Bessel function of the second kind. To construct any arrangement of vortices, it is important to describe the B-field behavior in the core more accurately since a logarithmically diverging field at small distances is not realistic enough for our attributions. Thankfully, expressions

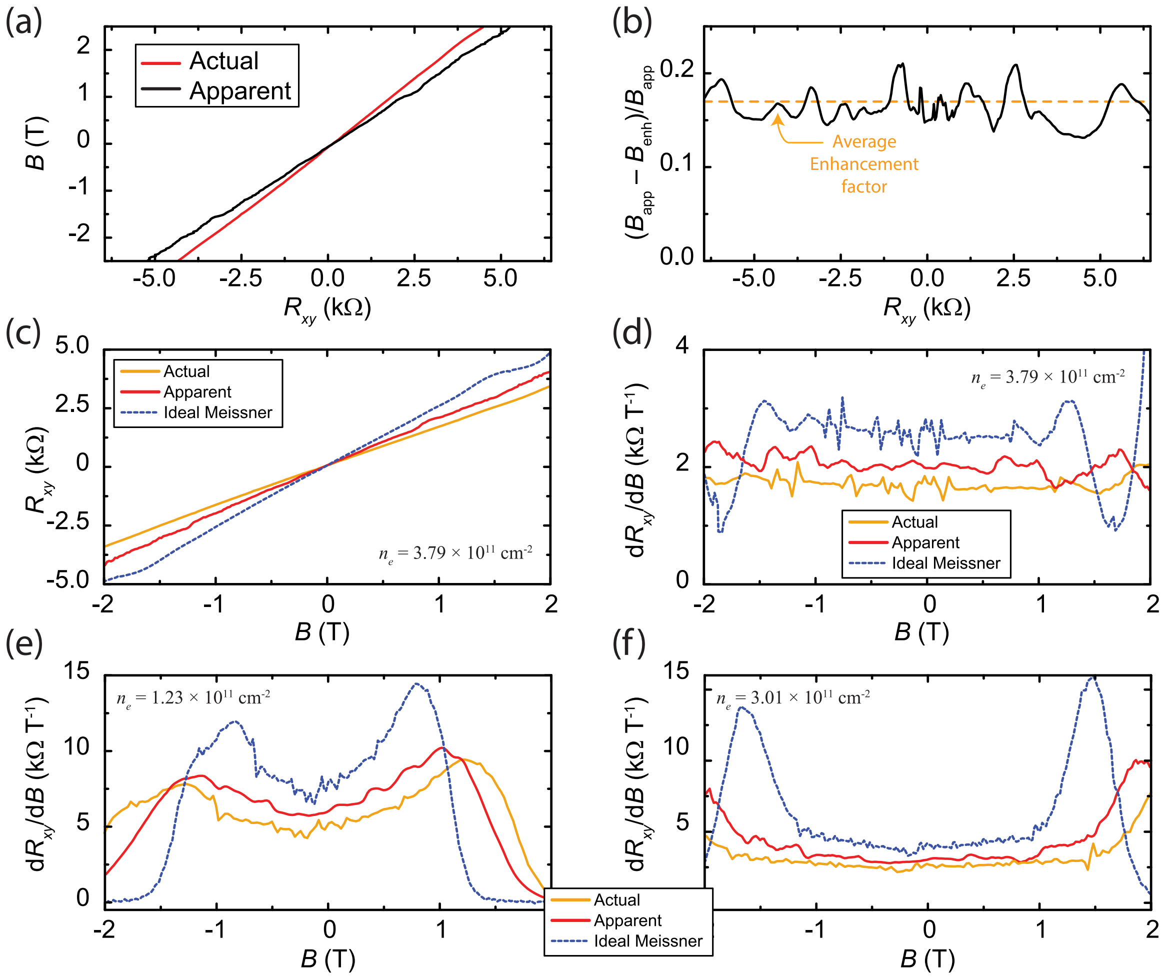

FIG. 5. (a) Data for a fixed electron density are compared to yield the fractional difference observed in regions adjacent to NbTiN slabs. The light blue region indicates the maximum extent of the validity of approximating the electron densities with low B-field resistance measurements. (b) The difference in the actual and apparent responses yield an average enhancement factor of ∼16.3%, determined from the low-field data. (c) Hall resistance data for a fixed electron density are compared for the actual and apparent cases (gold and red, respectively) as well as a simulated response curve for the event where the superconductors are in a pure Meissner state (dotted blue). (d)–(f) The first derivatives of the Hall resistance for three electron densities are shown to exhibit the extent of the validity of low-field electron density approximations.

for f have been derived for such small distances [47]:

$$f(r) \approx \frac{r}{2\xi}\left\{1 - \frac{r^2}{8\xi^2}\left[1 + \frac{B(0)}{B_{c2}}\right]\right\}. \tag{7}$$

In this case, $B(0)$ comes from a fixed value near the center of the vortex ($r \rightarrow 0$), found once $\mathbf{A}(r)$ is known via $\mathbf{A}(r) = \frac{1}{r}\int_0^r r'\mathbf{B}(r')dr'$. Equation (7), when substituted into Eqs. (4) and (5), enables one to numerically solve the more accurate form of $\mathbf{B}(r)$. This vortex field, specific to the NbTiN slabs, is plotted in the Supplemental Material [37], along with a short-range summation of periodic, neighboring vortices to demonstrate how these flux quanta, when arranged appropriately, allow a B field ($B_{c2} > B > B_{c1}$) to penetrate the NbTiN slab. By taking the limit of the summation in the case where the free energy of the vortex system is minimized [47,48], we obtain a triangular lattice of spacing: $(\frac{4}{3})^{1/4}\sqrt{\frac{\Phi_0}{B}}$ (which is also plotted in the Supplemental Material [37]).

One may now say that, for a reasonably low field (<1T), a triangular formation of Abrikosov vortices, with an intercore distance lower bound of the order of 10ξ, reduces the impact of the Meissner effect on local B-field enhancement by a factor with a lower bound of ∼2.5 to 3. This reduction is determined by taking the ratio of the horizontal scaling factors observed, one set of which is shown in Fig. 5(c). The inclusion of flux pinning and defects are beyond the scope of this analysis, but it is understood that ideal-case scenarios have inherent mathematical limitations. Though these observations have given an overall upper bound to the effect of Abrikosov vortices on the changes in Hall resistance and longitudinal resistivity, the inherent physics behind the enhanced field should not change in the event that other superconductors are used. Observations with type-I superconductors are warranted in future studies, despite critical temperatures being of millikelvin order. Furthermore, for applications to other two-dimensional materials, such as germanene, silicene, or phosphorene, appropriate experimental conditions must be established to measure the effect of any enhanced field, especially if a linear Hall effect at low B field is not present in the material.

V. CONCLUSIONS

In this paper, we investigated the effects of enhanced B fields resulting from adjacent type-II superconducting NbTiN slabs on the magnetotransport physics of narrow Hall bar devices fabricated from EG. The observed apparent changes in the magnetoresistances were found to have minimal contributions from device inhomogeneities, magnet hysteresis, electron density variations along the devices, and transient phenomena. The mixed state in type-II superconductors enabled the formation of Abrikosov vortices. When our determined λ_L was coupled with elements of GL theory, an approximation of the vortex densities at low field ($<$1T) became calculable. This analysis ultimately offered an upper bound to the effect of Abrikosov vortices on the changes in Hall resistance and longitudinal resistivity. The results and analyses presented here offer advancement in the application space of low-field, low-temperature technologies, where the local B-field enhancement can reduce future B-field requirements for a variety of devices.

ACKNOWLEDGMENTS

L.R.S. and A.F.R. designed the experiment and collected and analyzed data. L.R.S., C.-I.L., I-F.H., and D.S. fabricated samples. H.M.H., J.A.H., and A.F.R. conducted theoretical and simulation analyses. R.E.E., C.-T.L., P.B., D.B.N., and A.F.R. provided project guidance and oversight. All authors have contributed to the paper. L.R.S. acknowledges support from the National Science Foundation under the financial assistance Award No. NSF-1610953. The authors thank S. Payagala, G. J. Fitzpatrick, X. Wang, E. C. Benck, and the NIST Editorial Review Board for assistance with the internal NIST review process. The authors declare no competing interest.

[1] A. K. Geim and K. S. Novoselov, Nat. Mater. **6**, 183 (2007).
[2] A. H. Castro Neto, F. Guinea, N. M. R. Peres, K. S. Novoselov, and A. K. Geim, Rev. Mod. Phys. **81**, 109 (2009).
[3] K. S. Novoselov, V. I. Fal'ko, L. Colombo, P. R. Gellert, M. G. Schwab, and K. A. Kim, Nature (London) **490**, 192 (2012).
[4] S. Das Sarma, S. Adam, E. H. Hwang, and E. Rossi, Rev. Mod. Phys. **83**, 407 (2011).
[5] N. Tombros, C. Jozsa, M. Popinciuc, H. T. Jonkman, and B. J. Van Wees, Nature (London) **448**, 571 (2007).
[6] S. Cho, Y. F. Chen, and M. S. Fuhrer, Appl. Phys. Lett. **91**, 123105 (2007).
[7] M. Ohishi, M. Shiraishi, R. Nouchi, T. Nozaki, T. Shinjo, and Y. Suzuki, Jpn. J. Appl. Phys. **46**, L605 (2007).
[8] M. H. Liu, C. Gorini, and K. Richter, Phys. Rev. Lett. **118**, 066801 (2017).
[9] S. Ghosh and M. Sharma, J. Phys. Condens Mat. **21**, 292204 (2009).
[10] S. Chen, Z. Han, M. M. Elahi, K. M. Habib, L. Wang, B. Wen, Y. Gao, T. Taniguchi, K. Watanabe, J. Hone, and A. W. Ghosh, Science **353**, 1522 (2016).
[11] T. Taychatanapat, K. Watanabe, T. Taniguchi, and P. Jarillo-Herrero, Nat. Phys. **9**, 225 (2013).
[12] A. F. Rigosi, A. R. Panna, S. U. Payagala, M. Kruskopf, M. E. Kraft, G. R. Jones, B. Y. Wu, H. Y. Lee, Y. Yang, J. Hu, D. G. Jarrett, D. B. Newell, and R. E. Elmquist, IEEE Trans. Instrum. Meas. **68**, 1870 (2018).
[13] R. Ribeiro-Palau, F. Lafont, J. Brun-Picard, D. Kazazis, A. Michon, F. Cheynis, O. Couturaud, C. Consejo, B. Jouault, W. Poirier, and F. Schopfer, Nat. Nanotechnol. **10**, 965 (2015).
[14] J. Hu, A. F. Rigosi, M. Kruskopf, Y. Yang, B.-Y. Wu, J. Tian, A. R. Panna, H.-Y. Lee, S. U. Payagala, G. R. Jones, M. E. Kraft, D. G. Jarrett, K. Watanabe, T. Taniguchi, R. E. Elmquist, and D. B. Newell, Sci. Rep. **8**, 15018 (2018).
[15] A. Tzalenchuk, S. Lara-Avila, A. Kalaboukhov, S. Paolillo, M. Syväjärvi, R. Yakimova, O. Kazakova, T. J. B. M. Janssen, V. Fal'ko, and S. Kubatkin, Nat. Nanotechnol. **5**, 186 (2010).
[16] A. F. Rigosi and R. E. Elmquist, Semicond. Sci. Technol. **34**, 093004 (2019).
[17] K. Komatsu, C. Li, S. Autier-Laurent, H. Bouchiat, and S. Guéron, Phys. Rev. B **86**, 115412 (2012).
[18] S. Bhandari, G. H. Lee, K. Watanabe, T. Taniguchi, P. Kim, and R. M. Westervelt, Nano Lett. **20**, 4890 (2020).
[19] M. Popinciuc, V. E. Calado, X. L. Liu, A. R. Akhmerov, T. M. Klapwijk, and L. M. K. Vandersypen, Phys. Rev. B **85**, 205404 (2012).
[20] F. E. Schmidt, M. D. Jenkins, K. Watanabe, T. Taniguchi, and G. A. Steele, Nat. Commun. **9**, 1 (2018).
[21] H. J. Suominen, J. Danon, M. Kjaergaard, K. Flensberg, J. Shabani, C. J. Palmstrøm, F. Nichele, and C. M. Marcus, Phys. Rev. B **95**, 035307 (2017).
[22] F. K. de Vries, T. Timmerman, V. P. Ostroukh, J. van Veen, A. J. A. Beukman, F. Qu, M. Wimmer, B.-M. Nguyen, A. A. Kiselev, W. Yi, M. Sokolich, M. J. Manfra, C. M. Marcus, and L. P. Kouwenhouven, Phys. Rev. Lett. **120**, 047702 (2018).
[23] Commercial equipment, instruments, and materials are identified in this paper in order to specify the experimental procedure adequately. Such identification is not intended to imply recommendation or endorsement by the NIST or the U.S. government, nor is it intended to imply that the materials or equipment identified are necessarily the best available for the purpose.
[24] M. Kruskopf, D. M. Pakdehi, K. Pierz, S. Wundrack, R. Stosch, T. Dziomba, M. Götz, J. Baringhaus, J. Aprojanz, and C. Tegenkamp, 2D Mater. **3**, 041002 (2016).
[25] V. Panchal, Y. Yang, G. Cheng, J. Hu, M. Kruskopf, C.-I. Liu, A. F. Rigosi, C. Melios, A. R. Hight Walker, D. B. Newell, O. Kazakova, and R. E. Elmquist, Nat. Commun. Phys. **1**, 83 (2018).
[26] A. F. Rigosi, N. R. Glavin, C.-I. Liu, Y. Yang, J. Obrzut, H. M. Hill, J. Hu, H.-Y. Lee, A. R. Hight Walker, C. A. Richter, R. E. Elmquist, and D. B. Newell, Small **13**, 1700452 (2017).
[27] M. Kruskopf, A. F. Rigosi, A. R. Panna, D. K. Patel, H. Jin, M. Marzano, M. Berilla, D. B. Newell, and R. E. Elmquist, IEEE Trans. Electron Dev. **66**, 3973 (2019).
[28] M. Kruskopf, A. F. Rigosi, A. R. Panna, M. Marzano, D. Patel, H. Jin, D. B. Newell, and R. E. Elmquist, Metrologia **56**, 065002 (2019).

[29] A. A. Abrikosov, J. Phys. Chem. Solids **2**, 199 (1957).
[30] J. Bardeen and M. J. Stephen, Phys. Rev. **140**, A1197 (1965).
[31] K. Maki, J. Low Temp. Phys. **1**, 45 (1969).
[32] S. Sarkar, H. Zhang, J.-W. Huang, F. Wang, E. Bekyarova, C. N. Lau, and R. C. Haddon, Adv. Mater. **25**, 1131 (2013).
[33] E. Bekyarova, S. Sarkar, S. Niyogi, M. E. Itkis, and R. C. Haddon, J. Phys. D: Appl. Phys. **45**, 154009 (2012).
[34] A. F. Rigosi, M. Kruskopf, H. M. Hill, H. Jin, B.-Y. Wu, P. E. Johnson, S. Zhang, M. Berilla, A. R. Hight Walker, C. A. Hacker, D. B. Newell, and R. E. Elmquist, Carbon **142**, 468 (2019).
[35] S. Che, K. Jasuja, S. K. Behura, P. Nguyen, T. S. Sreeprasad, and V. Berry, Nano Lett. **17**, 4381 (2017).
[36] T. J. B. M. Janssen, A. Tzalenchuk, R. Yakimova, S. Kubatkin, S. Lara-Avila, S. Kopylov, and V. I. Fal'ko, Rev B **83**, 233402 (2011).
[37] See Supplemental Material at http://link.aps.org/supplemental/10.1103/PhysRevB.XX.XXXXXX for information on the upper critical field determination, layout of the COMSOL model, magnet hysteresis, device homogeneity, transient effects, electron density shifts with temperature, and vortex visualizations. Includes Ref. [49].
[38] N. R. Werthamer, E. Helfand, and P. C. Hohenberg, Phys. Rev. **147**, 295 (1966).
[39] A. Gurevich, Phys. Rev. B **67**, 184515 (2003).
[40] A. Klimov, W. Słysz, M. Guziewicz, V. Kolkovsky, I. Zaytseva, and A. Malinowski, Physica C Supercond. **536**, 35 (2017).
[41] M. N. Kunchur, Condens. Matter **4**, 54 (2019).
[42] N. S. Swails, Depairing current density in NbTiN superconducting films, Ph.D. dissertation, University of South Carolina, 2018 Retrieved from https://scholarcommons.sc.edu/etd/4918.
[43] J.-G. Caputo, L. Gozzelino, F. Laviano, G. Ghigo, R. Gerbaldo, J. Noudem, Y. Thimont, and P. Bernstein, J. Appl. Phys. **114**, 233913 (2013).
[44] D. Y. Vodolazov and I. L. Maksimov, Physica C **349**, 125 (2001).
[45] E. A. Matute, Am. J. Phys. **67**, 786 (1999).
[46] Z. Tan, C. Tan, L. Ma, G. T. Liu, L. Lu, and C. L. Yang, Phys. Rev. B **84**, 115429 (2011).
[47] M. Tinkham, *Introduction to Superconductivity* (Dover Publications, Mineola, 2004).
[48] H. Kleiner, L. M. Roth, and S. H. Autler, Phys. Rev. **133**, A1226 (1964).
[49] C. W. Liu, C. Chuang, Y. Yang, R. E. Elmquist, Y.-J. Ho, H.-Y. Lee, and C.-T. Liang, 2D. Mater. **4**, 025007 (2017).